

Effects of Stripe Width on the Porosity and Mechanical Performance of Additively Manufactured Ti-6Al-4V Parts

Arash Soltani-Tehrani^{1,2}, Mohammad Salman Yasin^{1,2}, Shuai Shao^{1,2}, Nima Shamsaei^{1,2,*}

¹Department of Mechanical Engineering, Auburn University, Auburn, AL, USA

²National Center for Additive Manufacturing Excellence (NCAME),
Auburn University, Auburn, AL, USA

*Corresponding author:

Email: shamsaei@auburn.edu

Phone: (334) 844 4839

Abstract

In laser powder bed fusion (L-PBF) additive manufacturing, parts are manufactured in a layer-by-layer pattern. In each layer, cross-sections can be scanned with or without partitioning by the laser, which are commonly known as “stripe” and “meander” patterns, respectively. Under the two scanning strategies, the thermal history experienced by the part can be considerably different. Accordingly, defect distribution, microstructure, and mechanical properties may be affected. In this study, two sets of Ti-6Al-4V specimens were fabricated using L-PBF: in one set, the tracks were partitioned in 5-mm stripes, while in the other set, they were partitioned at 100 mm resulting in no stripe seams in the cross-section. It was found that altering the stripe width can considerably affect the laser penetration depth, the defect content, and consequently fatigue performance. However, tensile strength was not much sensitive to changing the stripe width.

Keywords: Additive Manufacturing, Ti-6Al-4V, Stripe Width, L-PBF, Process Parameters

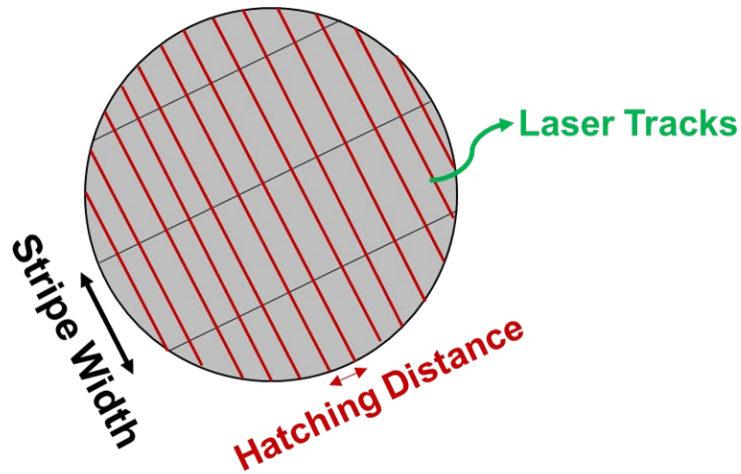
Introduction

In laser powder bed fusion (L-PBF) additive manufacturing, the part performance is dependent on the powder feedstock as well as design and process parameters. For instance, it has been reported that if the powder is reused or its characteristics such as the size and shape are altered, the initial process parameter set may be insufficient to achieve a full melting, and consequently, result in the formation of a larger population of gas-entrapped pores or lack of fusion defects [1–5].

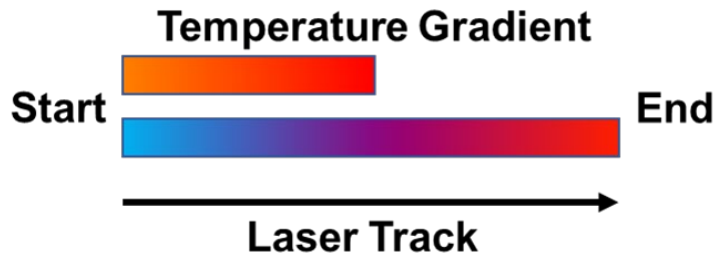
With identical process parameters, altering the geometry alone can result in the parts experiencing different thermal histories [6–8] and as a result different defect content and mechanical properties. For example, it has been stated that the fatigue resistance of parts machined from additively manufactured (AMed) 17-4 PH SS large blocks were superior to the ones obtained from oversized dog-bone parts [9]. Moreover, complex geometries such as lattice structures have been reported to give different mechanical properties when the size of the features is altered [10–12]. For instance, when the size of struts in lattices was decreased, a higher surface roughness, less ductility, and ultimate tensile strength were noted in Ref. [13]. Therefore, adjusting the process parameters to achieve a consistent thermal history between different components, is essential to attain comparable part performance especially when complex geometries with different features are fabricated [10,14].

Although many AM process parameters can influence the microstructure and defect content of parts, including but not limited to laser power, scanning speed, hatching distance, stripe width, layer thickness, laser spot size, inert gas flow speed and pressure, inert gas type, build plate preheating temperature [14–25], there only exist studies in the literature to quantify a few of them (such as laser power and scan speed). The precise effect of other parameters remains elusive.

Stripe width is among the parameters whose effect on part performance is less well known. As seen in Fig. 1(a), the stripes can partition the scanned area so that the laser tracks are not appreciably large. The shorter molten tracks are believed to result in smaller temperature gradients within each scan track (see Fig. 1(b)). Specifically, when the laser is moving along long tracks, the temperature at the onset of the track will be much less than the end of the track, resulting in a higher temperature gradient.



(a)



(b)

Fig. 1 (a) Schematic illustration of the stripe width, hatching distance, and laser tracks during the L-PBF process, and (b) temperature gradient in the short and long laser tracks.

Therefore, this study aims to investigate the effects of fabricating specimens with and without striping for L-PBF Ti-6Al-4V (Ti64). Following the introduction, the experimental program employed to characterize the part performance will be explained. Results will be subsequently presented in the order of defect content, microstructure, melt pool penetration depth, hardness, and tensile and fatigue properties. In addition, the observations on the experimental results will be discussed further, and lastly, some major conclusions will be drawn based on the results and discussions.

Experimental Program

In this study, plasma-atomized Ti-6Al-4V (Ti64) from AP&C, a GE Additive Company with an initial particle size distribution (PSD) of 15-53 μm was used. Two sets of specimens were fabricated in one print in an argon environment using EOS M290, an L-PBF AM machine. Ti64 performance process parameters were used to fabricate all parts including the infill laser power (P) of 280 W, scanning speed (V) of 1200 mm/s, hatching distance (h) of 0.14 mm, and 30 μm layer thickness (t) resulting in 55.6 J/mm^3 energy density. All the process conditions for both sets of specimens were kept the same and the only difference was that one set was fabricated using a stripe width of 5 mm (hereon referred to as default) and the other fabricated with 100-mm stripe width (hereon referred to as modified) to ensure there would be no partition on the cross-section of the parts (see Fig. 2 for the layout). It needs to be specified that these two strategies are also known as “stripe” and “meander” scan patterns, respectively.

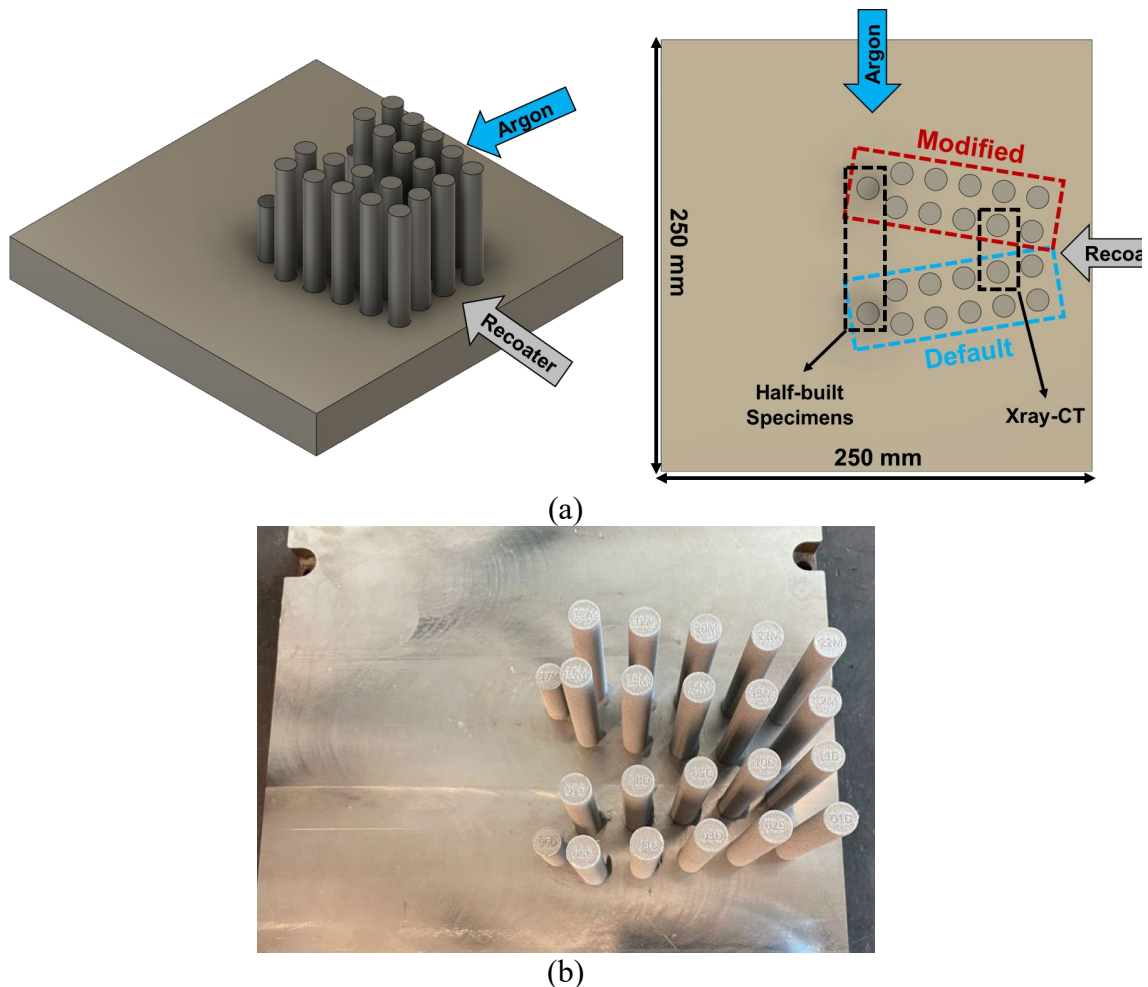


Fig. 2 (a) Schematic illustration of the build layout that was used for L-PBF Ti64 fabrication, and (b) as-fabricated parts. Default and modified specimens are respectively enclosed with blue and red dashed boxes.

On the build plate, there were 10 cylindrical specimens in each set. In addition, one specimen per condition was manufactured with a height half of the full cylinders for

microstructural analyses to represent the gage section of the fatigue specimens. These parts are illustrated as “half-built specimens” in Fig. 2(a). All specimens were located near the feedstock and center to minimize the effects of powder segregation on the mechanical properties [26]. All parts were manufactured on 3 mm support structures for straightforward removal of the build plate. After fabrication, the half-built specimens were removed in their non-heat-treated (NHT) condition, and the remainder were stress relieved (SR) on the build plate. The SR treatment was conducted at 900 °C for 1 hour in an argon environment followed by furnace cooling.

All cylinders were machined to the geometry of fatigue specimens according to ASTM E466 (see Fig. 3) with a gage diameter of 0.2 inches (~5 mm) after SR [27]. After machining, tensile tests were conducted on two specimens from each set on the same geometry with a procedure based on ASTM E8 [28]. Tensile tests were carried out in displacement-control mode with a nominal strain rate of 0.001 mm/mm/s in an MTS Landmark servohydraulic load frame equipped with a 100 kN load cell. Before tests, the gage length of specimens was marked to measure the percent elongation to failure (%EL) after the specimen fractures. In addition, only the first 0.05 mm/mm (5%) strain of each test was performed with an extensometer for an accurate measure of yield strength (YS). Force-controlled fully-reversed ($R = -1$) fatigue tests were also conducted using an MTS Bionix Tabletop load frame with a 25 kN load cell at two different stress levels according to ASTM E466 [27].

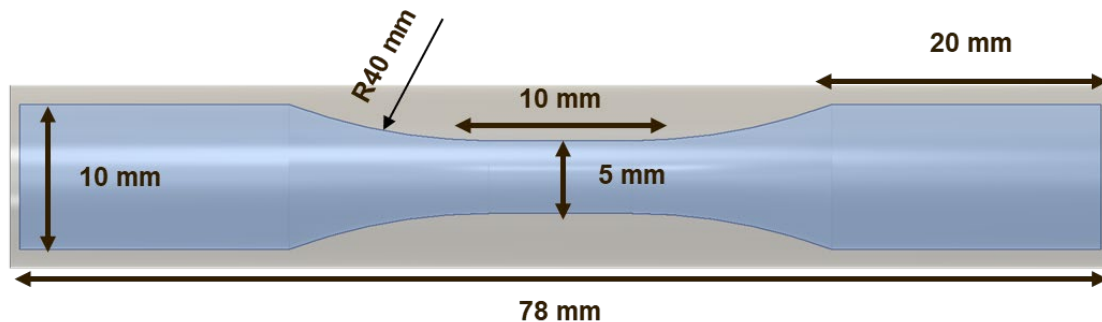


Fig. 3 The geometry of fatigue specimens according to ASTM E466. All dimensions are in millimeters.

Two specimens were randomly selected for X-ray Computed Tomography (XCT) analyses. The XCT was conducted via the Zeiss Xradia 620 Versa with a voltage, current, and voxel size of 140 kV, 150 μ A, and 6 μ m, respectively. After scanning, image slices were reconstructed using the built-in software. To ensure the reliability of the defect analysis and exclude the false defect detection from noise in the data, any defects smaller than 10 μ m were discarded. The reason to exclude such defects was that small defects have usually less probability of fatigue cracks nucleation [14]. In addition, 3D visualizations of the defect distribution within the specimens were generated using DragonFly software [29].

As previously mentioned, the half-built specimens were used for microstructural analyses. At first, the specimens were cut in transverse and normal directions (TD and ND) and etched using the modified Krolls' reagent (10% HF, 10% HNO₃, and 80% distilled water). Afterward, the microstructure, melt pool boundaries and laser penetration depth were observed using a Keyence VHX-6000 digital microscope. In addition, hardness tests were conducted on the cross-section of half-built specimens via a LECO LCR 500 with a load rate of 60 μ N/s. The hardness test results are presented in the Rockwell C (HRC) scale as suggested in ASTM E18 [30].

Results and Discussions

As seen in Fig. 4(a) and (b), the microstructure in both specimens consists of an $\alpha+\beta$ Widmanstätten structure, which seems not to be affected by the stripe width. The $\alpha+\beta$ microstructure in the L-PBF Ti64 parts is mainly derived from the decomposition of α' to $\alpha+\beta$ [31,32]. In addition, the prior β grains were found to be elongated toward the build plate as the heat is mainly dissipated in this direction. The similar microstructure observed in each specimen can be because both specimens were manufactured using the same powder with comparable layer time intervals. Therefore, not much difference in the grain structure is expected.

As labeled on the image, the melt pool depth was also calculated by measuring a minimum of 10 melt pools per condition, which showed $210 \pm 24 \mu\text{m}$ and $156 \pm 5 \mu\text{m}$ laser penetration depth for the default and modified conditions, respectively. The changes in laser penetration depth can be correlated with stripe width which should have resulted to some extent different thermal histories. It seems that when shorter tracks were used (i.e., default), there was excessive heat input especially at laser turning spots [33]. The higher heat input should have resulted in deeper melt pools, which were on average $\sim 35\%$ larger for the default condition as compared with the modified one.

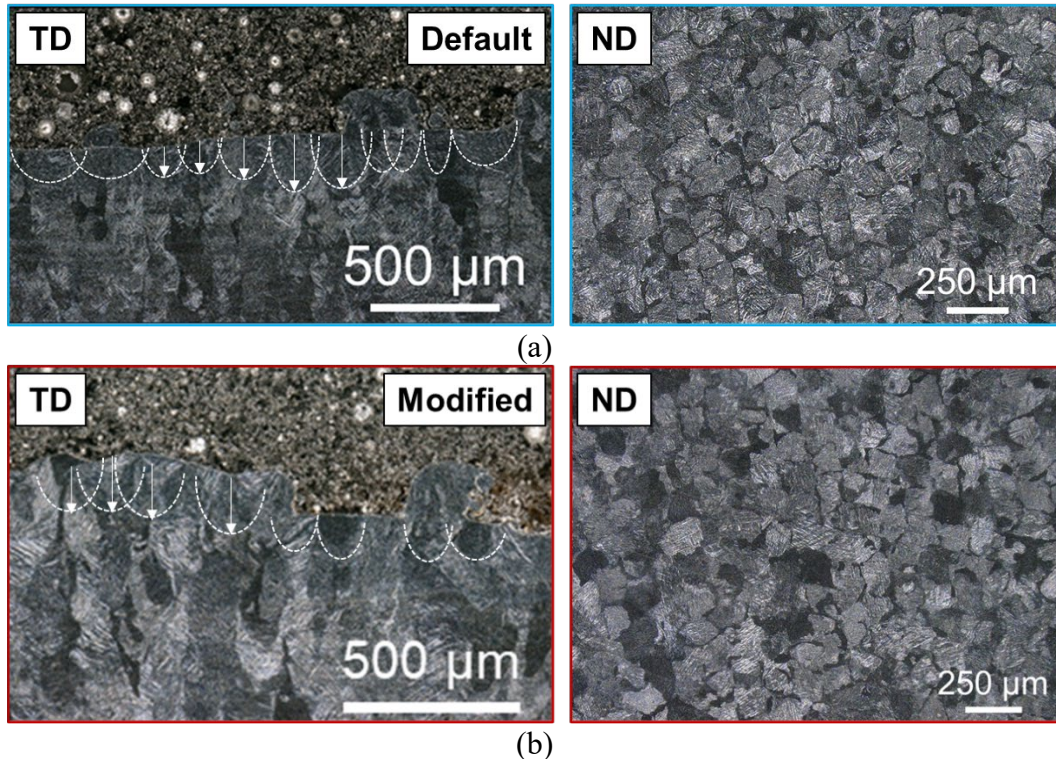


Fig. 4 The microstructure and melt pool shapes in L-PBF Ti64 fabricated via (a) default and (b) modified stripe width in their NHT conditions for both transverse and normal directions (TD and ND). The arrows show the melt pool depth along the building direction.

As seen in Fig. 5, the defect distributions in both specimens are shown with 3D visualizations. It seems that there are a larger number of defects when the default scan pattern was used. However, some large defects are also evident in the case of the modified scan pattern. Observing more defects in the default specimen was quite interesting. As previously explained,

smaller stripes are supposed to result in a uniform temperature distribution along the tracks. However, it seems that the presence of more turns and excessive energy input at the beginning and end of shorter tracks (as the laser slows down to turn) can result in the formation of keyhole pores in such locations. This observation was consistent with Ref. [33] where a higher probability of keyholes was reported in laser turning spots in serpentine strategies.

The observations of more defects near the stripe boundaries and in some cases keyholes have been attributed to the fast cooling rates in the L-PBF process, having less time for the molten material to fill in the empty spaces [34]. The authors are aware of an option known as “skywriting” in the EOS M290 which supposedly controls the laser turning to occur outside of the hatch lines to prevent overheating at the onset and end of each track. However, Martin et al. [33] stated that skywriting still cannot alleviate this issue due to the physical limitations of mirror-based scanning setups. Alternatively, varying laser power along the tracks was introduced as the efficient solution to make the energy density uniform at turn spots [33].

Tensile stress-strain and stress-displacement curves are reported in Fig. 6. As seen in this figure, tensile properties including the ultimate tensile strength (UTS), yield strength (YS), and percent elongation to failure (%EL) were almost comparable for both cases. The UTS was ~1013-1014 MPa for both conditions. The YS was somewhat higher in the modified specimens, which can be attributed to slightly finer lath martensite thickness due to higher cooling rates in these specimens. Additionally, the %EL was almost comparable for both scan patterns. In general, consistent with the similar microstructures in both specimen sets, similar tensile properties were observed.

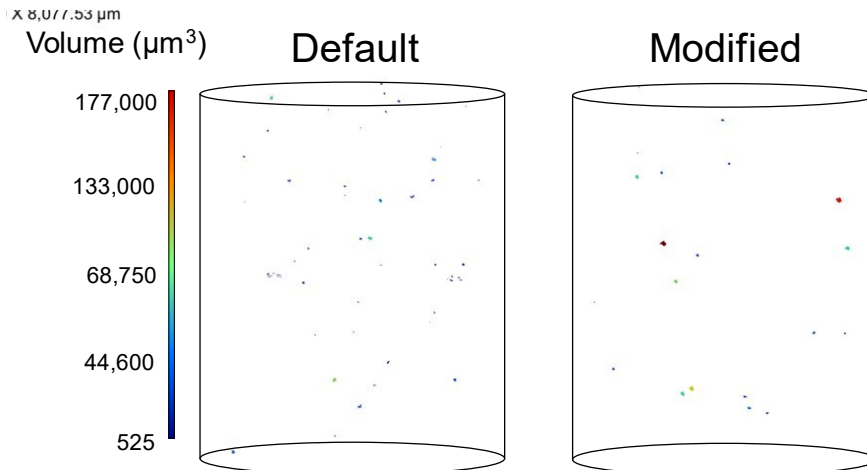
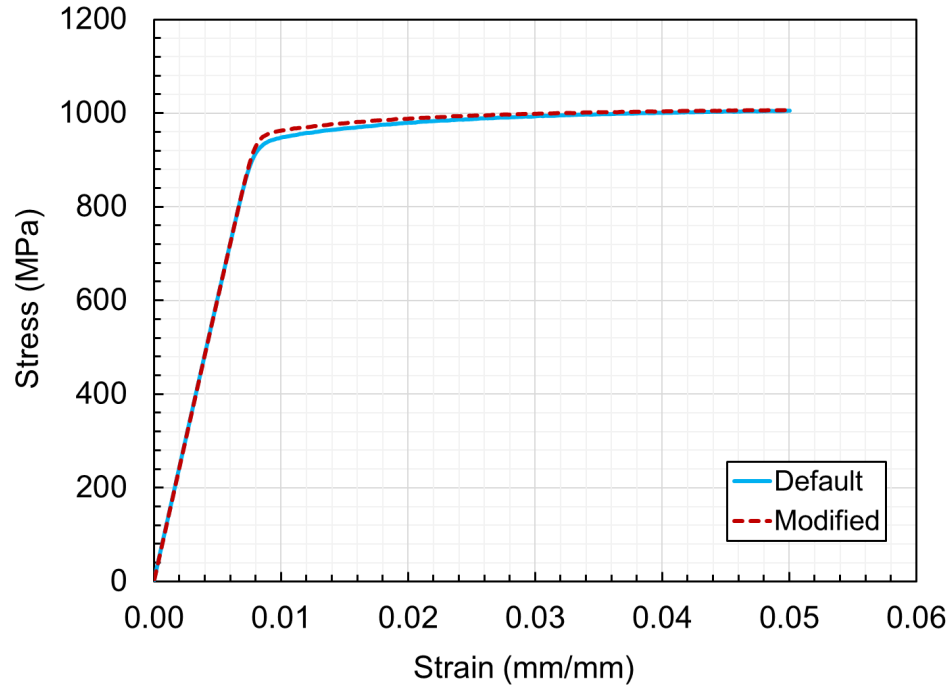
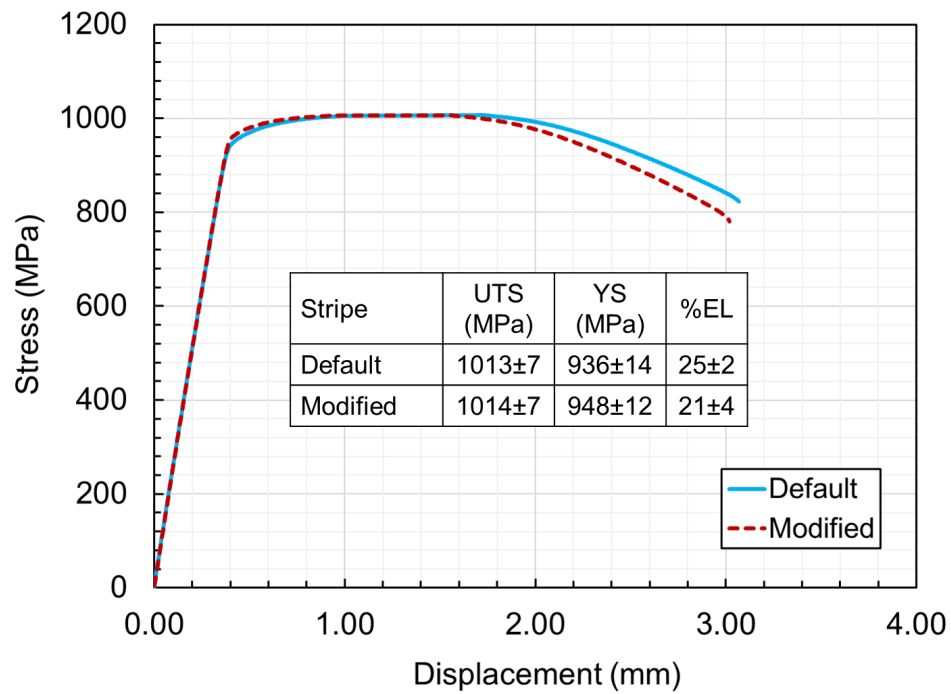


Fig. 5 3D visualizations of defect content in L-PBF Ti64 specimens manufactured using default and modified scan patterns.



(a)



(b)

Fig. 6 (a) Engineering stress-engineering strain and (b) engineering stress-displacement curves for L-PBF Ti64 parts fabricated using default and modified patterns in machined surface conditions.

Hardness tests were also conducted for both default and modified specimens. As seen in Fig. 7, it was found that there is no difference in the HRC results. The similar HRC well correlates

with the similar tensile properties and microstructure that were previously discussed. Therefore, it may be overall assumed that changing the stripe width does not alter the microstructure.

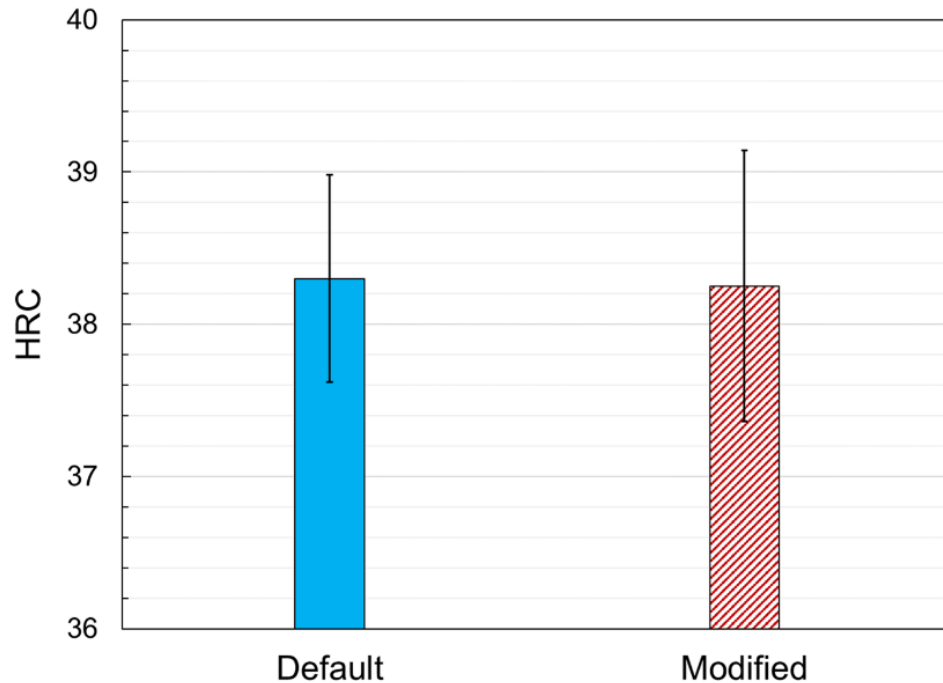


Fig. 7 Rockwell C hardness (HRC) values for both default and modified L-PBF Ti64 specimens in their NHT conditions.

Fully-reversed fatigue tests were conducted on the specimens fabricated using the default and modified scan patterns and reported in Fig. 8. Tests were conducted at two stress levels (i.e., 700 and 600 MPa) to include the mid-cycle and high-cycle fatigue regimes. It was noticed that using a modified scan pattern can result in somewhat higher fatigue performance at lower stress levels (i.e., high-cycle fatigue). However, as the stress level was increased, the difference between fatigue lives was diminished. This behavior can be explained by the fact that at lower stress levels, the majority of fatigue life is spent at crack nucleation whereas, at higher stress levels, it is mainly spent at crack growth [35].

As the crack growth behavior is more dependent on the microstructure and no difference was noted in the microstructure of the parts fabricated using default and modified scan patterns (see Fig. 4), negligible variation between fatigue lives can be expected. The high-cycle fatigue regime, however, is typically governed by the defect content in the AMed parts. As a result, it may be assumed that critical defects resulting in fatigue failures were typically smaller in the specimens manufactured using a modified scan pattern. As previously explained, due to excessive energy inputs at the onset and end of laser tracks in default specimens, some large pores can be present which are detrimental to fatigue resistance. A summary of all fatigue tests is also reported in Table 1.

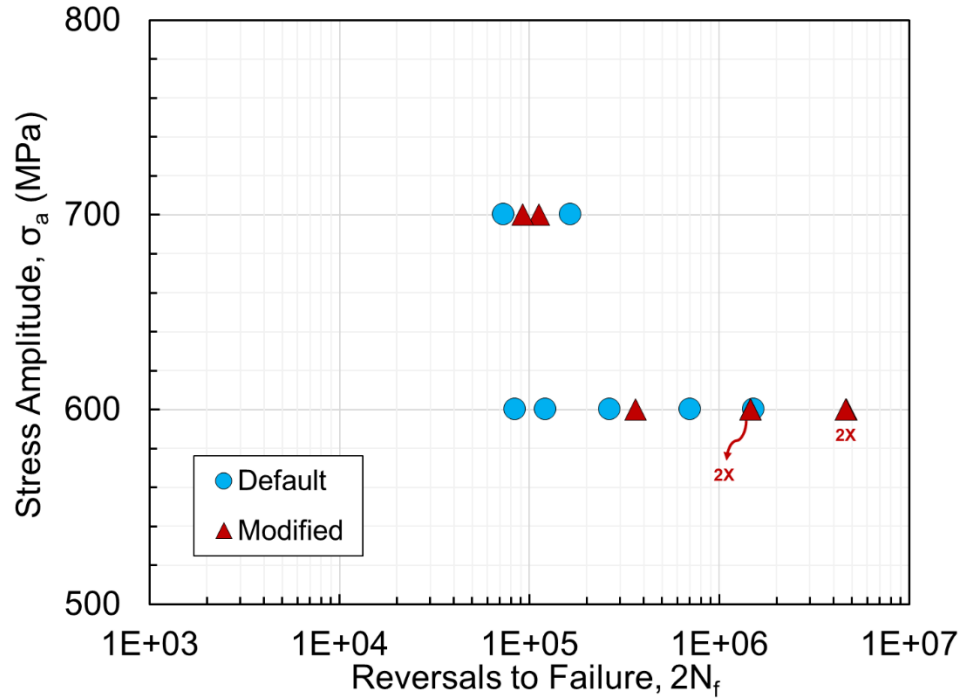


Fig. 8 Fatigue performance of L-PBF Ti64 parts fabricated using default and modified scan patterns in machined surface condition.

Table 1 A summary of fully-reversed force-controlled fatigue tests for L-PBF Ti64 specimens in machined surface condition and manufactured using default and modified scan patterns.

| Specimen ID | σ_a (MPa) | $2N_f$ (Reversals) | Scan Pattern |
|-------------|------------------|--------------------|--------------|
| 05D | 600 | 1,513,966 | Default |
| 03D | 600 | 703,184 | |
| 09D | 600 | 121,602 | |
| 02D | 600 | 284,200 | |
| 04D | 600 | 265,520 | |
| 07D | 700 | 165,472 | |
| 08D | 700 | 73,312 | |
| 18M | 600 | 1,454,378 | Modified |
| 20M | 600 | 4,687,934 | |
| 14M | 600 | 4,615,468 | |
| 21M | 600 | 1,458,260 | |
| 19M | 600 | 363,442 | |
| 16M | 700 | 111,772 | |
| 15M | 700 | 91,796 | |

The fracture surfaces of some specimens were investigated to compare the defect sizes resulting in fatigue failures. It needs to be specified that all fracture surfaces were investigated however only two of them are presented here. As seen in Fig. 9, one specimen from each set is shown. It can be seen that the specimen fabricated using the modified scan pattern had higher

fatigue life. The equivalent defect sizes were evaluated based on Murakami's approach which considers the $\sqrt{\text{area}}$ of the defect [36,37]. It can be noted that the default specimen had a smaller crack initiation site however it was at the surface resulting in considerably smaller fatigue life. In the case of modified, the defect was away from the surface.

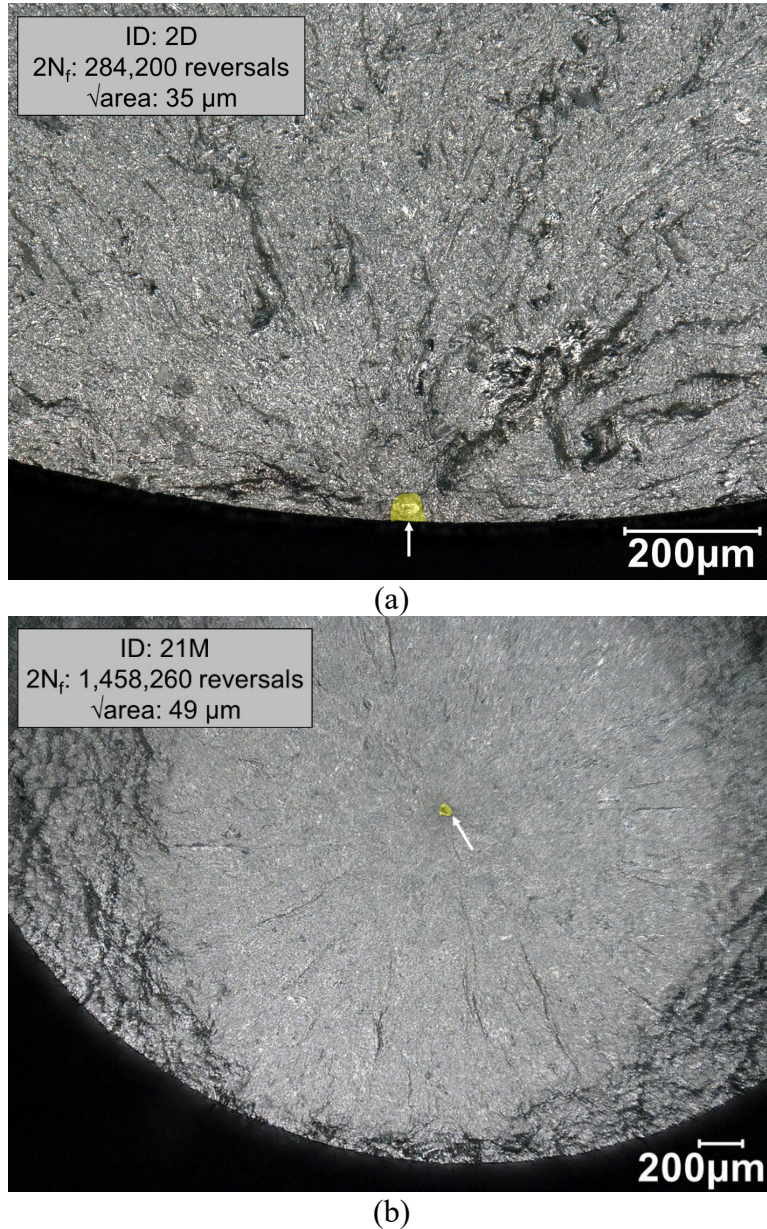


Fig. 9 Fracture surfaces of L-PBF Ti64 specimens manufactured using (a) default and (b) modified scan patterns. Both specimens were tested at 600 MPa.

To have a better estimate of all the critical defect sizes that resulted in fatigue failures, the $\sqrt{\text{area}}$ of critical defects was plotted on a Gumbel curve. As reported in Ref. [38], the critical defect size obtained by $\sqrt{\text{area}}$ follows the extreme value distribution which is shown in Fig. 10. The reduced variate (Y), shown in this figure, is calculated by $Y = -\ln(-\ln(i/N+1))$, where i is the rank of the defect based on its size and N is the total number of defects investigated [39]. From this

figure, it can be noticed that for a majority of tests, there is a significant overlap in defect sizes between the two sets. However, for some specimens, some larger defects were also observed in the case of default scan pattern whereas smaller defect sizes were seen in the counterpart specimens manufactured using modified scan pattern.

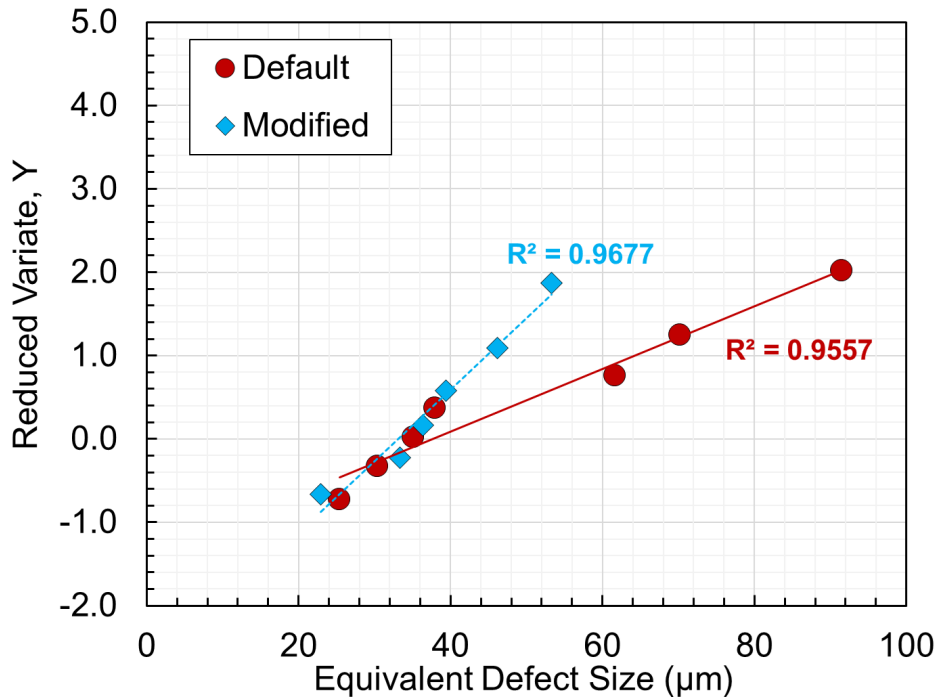


Fig. 10 Extreme value distribution for L-PBF Ti64 specimens manufactured using default and modified scan patterns.

Conclusions

In this study, two sets of L-PBF Ti64 specimens were fabricated by utilizing different stripe widths during scans, one with a 5-mm stripe as default, and another one with 100 mm as the modified (also known as meander scan pattern). Following conclusions can be drawn based on the experimental results:

- Using a smaller partition size may result in larger laser penetration depth due to excessive energy input in laser turn spots.
- The number of defects increased with decreasing the stripe width which was attributed to more frequent laser turn spots.
- Stripe width variations resulted in negligible changes in the microstructure, HRC, and tensile properties.
- Fatigue performance was to some extent improved at lower stress levels (i.e., high-cycle fatigue regime) when stripe width was enlarged. However, as the stress level was increased, the difference between fatigue lives was diminished.

In summary, it seems that altering the stripe width can considerably affect the defect content of AMed parts. This difference can be even further pronounced when more complex geometries are fabricated. Therefore, more investigation into the effects of stripe width is indeed

recommended. It is also important to study the effects of stripe width in large components where residual stress during fabrication might be a challenge.

Acknowledgment

This material is based upon work partially supported by the National Institute of Standards and Technology (NIST) under Award No. 70NANB19H170 and National Science Foundation (NSF) under Grant No. 1919818.

References

- [1] P.E. Carrion, A. Soltani-Tehrani, S.M. Thompson, N. Shamsaei, Effect of Powder Degradation on the Fatigue Behavior of Additively Manufactured As-Built Ti-6Al-4V, *Solid Free. Fabr. Proc.* (2018).
- [2] A. Soltani-Tehrani, J. Pegues, N. Shamsaei, Fatigue behavior of additively manufactured 17-4 PH stainless steel: The effects of part location and powder re-use, *Addit. Manuf.* 36 (2020) 101398. doi:10.1016/j.addma.2020.101398.
- [3] P. Dastranjy Nezhadfar, A. Soltani-Tehrani, A. Sterling, N. Tsolas, N. Shamsaei, Effects of Powder Recycling on the Mechanical Properties of Additively Manufactured Stainless Steel 17-4PH, *Solid Free. Fabr. Proc.* (2018) 1292–1300.
- [4] S.E. Brika, M. Letenneur, C.A. Dion, V. Brailovski, Influence of particle morphology and size distribution on the powder flowability and laser powder bed fusion manufacturability of Ti-6Al-4V alloy, *Addit. Manuf.* 31 (2020) 100929. doi:10.1016/j.addma.2019.100929.
- [5] J.H. Tan, W.L.E. Wong, K.W. Dalgarno, An overview of powder granulometry on feedstock and part performance in the selective laser melting process, *Addit. Manuf.* 18 (2017) 228–255. doi:10.1016/j.addma.2017.10.011.
- [6] S.M.J. Razavi, B. Van Hooreweder, F. Berto, Effect of build thickness and geometry on quasi-static and fatigue behavior of Ti-6Al-4V produced by Electron Beam Melting, *Addit. Manuf.* 6 (2020) 101426. doi:10.1016/j.addma.2020.101426.
- [7] D. Barba, C. Alabort, Y.T. Tang, M.J. Viscasillas, R.C. Reed, E. Alabort, On the size and orientation effect in additive manufactured Ti-6Al-4V, *Mater. Des.* 186 (2020) 108235. doi:10.1016/j.matdes.2019.108235.
- [8] C. Phutela, N.T. Aboulkhair, C.J. Tuck, I. Ashcroft, The effects of feature sizes in selectively laser melted Ti-6Al-4V parts on the validity of optimised process parameters, *Materials (Basel)*. 13 (2020) 117. doi:10.3390/ma13010117.
- [9] R. Shrestha, N. Shamsaei, M. Seifi, N. Phan, An investigation into specimen property to part performance relationships for laser beam powder bed fusion additive manufacturing, *Addit. Manuf.* 29 (2019) 100807. doi:10.1016/j.addma.2019.100807.
- [10] A. Soltani-Tehrani, S. Lee, M. Reza, V. Sereshk, N. Shamsaei, Effects of Unit Cell Size on the Mechanical Performance of Additive Manufactured Lattice Structures, in: *Proc. 30th Annu. Int. Solid Free. Fabr. Symp. Addit. Manuf. Conf.*, 2019: pp. 2254–2262.
- [11] Z. Xiao, Y. Yang, R. Xiao, Y. Bai, C. Song, D. Wang, Evaluation of topology-optimized

- lattice structures manufactured via selective laser melting, *Mater. Des.* 143 (2018) 27–37. doi:10.1016/j.matdes.2018.01.023.
- [12] M.R. Vaziri Sereshk, K. Triplett, C. St. John, K. Martin, S. Gorin, A. Avery, E. Byer, C.S. Pierre, A. Soltani-Tehrani, N. Shamsaei, A Computational and Experimental Investigation into Mechanical Characterizations of Strut-Based Lattice Structures, in: *Proc. 30th Annu. Int. Solid Free. Fabr. Symp. Addit. Manuf. Conf.*, 2019: pp. 2196–2207.
- [13] A.M. Roach, B.C. White, A. Garland, B.H. Jared, J.D. Carroll, B.L. Boyce, Size-dependent stochastic tensile properties in additively manufactured 316L stainless steel, *Addit. Manuf.* 32 (2020) 101090. doi:10.1016/j.addma.2020.101090.
- [14] A. Soltani-Tehrani, R. Shrestha, N. Phan, M. Seifi, N. Shamsaei, Establishing Specimen Property to Part Performance Relationships for Laser Beam Powder Bed Fusion Additive Manufacturing, *Int. J. Fatigue.* (2021) 106384. doi:10.1016/j.ijfatigue.2021.106384.
- [15] P.D. Nezhadfar, K. Anderson-Wedge, S. Dandiewicz, N. Phan, S. Shao, N. Shamsaei, Improved High Cycle Fatigue Performance of Additively Manufactured 17-4 PH Stainless Steel via In-Process Refining Micro-/Defect-Structure (Under Review), *Addit. Manuf.* (2020).
- [16] A. Keshavarzkermani, R. Esmaeilzadeh, U. Ali, P.D. Enrique, Y. Mahmoodkhani, N.Y. Zhou, A. Bonakdar, E. Toyserkani, Controlling mechanical properties of additively manufactured hastelloy X by altering solidification pattern during laser powder-bed fusion, *Mater. Sci. Eng. A.* 762 (2019) 138081. doi:10.1016/j.msea.2019.138081.
- [17] P.D. Nezhadfar, A. Soltani-Tehrani, N. Shamsaei, Effect of Preheating Build Platform on Microstructure and Mechanical Properties of Additively Manufactured 316L Stainless Steel, in: *Proc. 30th Annu. Int. Solid Free. Fabr. Symp. Addit. Manuf. Conf.*, 2019: pp. 415–425.
- [18] P.D. Nezhadfar, N. Shamsaei, N. Phan, Enhancing ductility and fatigue strength of additively manufactured metallic materials by preheating the build platform, *Fatigue Fract. Eng. Mater. Struct.* 44 (2021) 257–270. doi:10.1111/ffe.13372.
- [19] M. Masoomi, A. Soltani-Tehrani, N. Shamsaei, S.M. Thompson, Convection Heat Transfer Coefficients for Laser Powder Bed Fusion, in: *Proc. 29th Annu. Int. Solid Free. Fabr. Symp. Addit. Manuf. Conf.*, 2018: pp. 1686–1693.
- [20] R. Cunningham, S.P. Narra, T. Ozturk, J. Beuth, A.D. Rollett, Evaluating the Effect of Processing Parameters on Porosity in Electron Beam Melted Ti-6Al-4V via Synchrotron X-ray Microtomography, 68 (2016) 765–771. doi:10.1007/s11837-015-1802-0.
- [21] J.P. Oliveira, A.D. LaLonde, J. Ma, Processing parameters in laser powder bed fusion metal additive manufacturing, *Mater. Des.* 193 (2020) 1–12. doi:10.1016/j.matdes.2020.108762.
- [22] A. Yadollahi, N. Shamsaei, S.M. Thompson, D.W. Seely, Effects of process time interval and heat treatment on the mechanical and microstructural properties of direct laser deposited 316L stainless steel, *Mater. Sci. Eng. A.* 644 (2015) 171–183. doi:10.1016/j.msea.2015.07.056.
- [23] A. Keshavarzkermani, E. Marzbanrad, R. Esmaeilzadeh, Y. Mahmoodkhani, U. Ali, P.D. Enrique, N.Y. Zhou, A. Bonakdar, E. Toyserkani, An investigation into the effect of process

- parameters on melt pool geometry, cell spacing, and grain refinement during laser powder bed fusion, *Opt. Laser Technol.* (2019). doi:10.1016/j.optlastec.2019.03.012.
- [24] R. Cunningham, C. Zhao, N. Parab, C. Kantzos, J. Pauza, K. Fezzaa, T. Sun, A.D. Rollett, Keyhole threshold and morphology in laser melting revealed by ultrahigh-speed x-ray imaging, *Science* (80-.). 363 (2019) 849–852. doi:10.1126/science.aav4687.
- [25] B. Diehl, A. Nassar, Reducing near-surface voids in metal (Ti-6Al-4V) powder bed fusion additive manufacturing: the effect of inter-hatch travel time, *Addit. Manuf.* 36 (2020) 101592. doi:10.1016/j.addma.2020.101592.
- [26] G. Jacob, C.U. Brown, A. Donmez, The Influence of Spreading Metal Powders with Different Particle Size Distributions on the Powder Bed Density in Laser-Based Powder Bed Fusion Processes, *NIST Adv. Manuf. Ser.* (2018) 100–17. doi:10.6028/NIST.AMS.100-17.
- [27] ASTM International, E466 Standard Practice for Conducting Force Controlled Constant Amplitude Axial Fatigue Tests of Metallic Materials, West Conshohocken, PA; ASTM Int. (2015). doi:10.1520/E0466-15.2.
- [28] ASTM International, E8/E8M Standard Test Methods for Tension Testing of Metallic Materials, West Conshohocken, PA; ASTM Int. (2016). doi:https://doi.org/10.1520/E0008_E0008M-13.
- [29] Object Research Systems (ORS) Inc, Dragonfly 2020.2 [Computer software], (2020). <http://www.theobjects.com/dragonfly>.
- [30] ASTM International, E18-20 Standard Test Methods for Rockwell Hardness of Metallic Materials, West Conshohocken, PA; ASTM Int. (2020). doi:10.1520/E0018-14.2.
- [31] J.W. Pegues, S. Shao, N. Shamsaei, N. Sanaei, A. Fatemi, D.H. Warner, P. Li, N. Phan, Fatigue of additive manufactured Ti-6Al-4V, Part I: The effects of powder feedstock, manufacturing, and post-process conditions on the resulting microstructure and defects, *Int. J. Fatigue.* 132 (2020) 105358. doi:10.1016/j.ijfatigue.2019.105358.
- [32] R. Molaei, A. Fatemi, N. Sanaei, J. Pegues, N. Shamsaei, S. Shao, P. Li, D.H. Warner, N. Phan, Fatigue of additive manufactured Ti-6Al-4V, Part II: The relationship between microstructure, material cyclic properties, and component performance, *Int. J. Fatigue.* 132 (2020) 105363. doi:10.1016/j.ijfatigue.2019.105363.
- [33] A.A. Martin, N.P. Calta, S.A. Khairallah, J. Wang, P.J. Depond, A.Y. Fong, V. Thampy, G.M. Guss, A.M. Kiss, K.H. Stone, C.J. Tassone, J. Nelson Weker, M.F. Toney, T. van Buuren, M.J. Matthews, Dynamics of pore formation during laser powder bed fusion additive manufacturing, *Nat. Commun.* 10 (2019) 1–10. doi:10.1038/s41467-019-10009-2.
- [34] M.A. Groeber, E. Schwalbach, S. Donegan, K. Chaput, T. Butler, J. Miller, Application of characterization, modelling, and analytics towards understanding process-structure linkages in metallic 3D printing, *IOP Conf. Ser. Mater. Sci. Eng.* 219 (2017). doi:10.1088/1757-899X/219/1/012002.
- [35] R.I. Stephens, A. Fatemi, R.R. Stephens, H.O. Fuchs, *Metal fatigue in engineering*, John Wiley & Sons, 2000.
- [36] Y. Murakami, *Metal Fatigue- Effects of Small Defects and Nonmetallic Inclusions*, 2002.

doi:10.4293/108680811X13125733356710.

- [37] R. Shrestha, J. Simsiriwong, N. Shamsaei, Fatigue behavior of additive manufactured 316L stainless steel parts: Effects of layer orientation and surface roughness, *Addit. Manuf.* 28 (2019) 23–38. doi:10.1016/j.addma.2019.04.011.
- [38] Z.M. Jian, G.A. Qian, D.S. Paolino, A. Tridello, F. Berto, Y.S. Hong, Crack initiation behavior and fatigue performance up to very-high-cycle regime of AlSi10Mg fabricated by selective laser melting with two powder sizes, *Int. J. Fatigue.* 143 (2021) 106013. doi:10.1016/j.ijfatigue.2020.106013.
- [39] ASTM International, E2283 Standard Practice for Extreme Value Analysis of Nonmetallic Inclusions in Steel and Other Microstructural Features, West Conshohocken, PA; ASTM Int. (2019). doi:10.1520/E2283-08R19.1.